Bioactive Materials 39 (2024) 443–455

Contents lists available at ScienceDirect

Bioactive Materials

journal homepage: www.keaipublishing.com/en/journals/bioactive-materials

Mechanically skin-like and water-resistant self-healing bioelastomer for high-tension wound healing

Jinyi Huang [a,b,1], Hongying Chen [a,1], Zenghui Jia [a,b,1], Xingqi Song [a], Sinan Wang [a], Baoshuai Bai [a], Jian Wang [a,***], Junfeng Zhang [a,**], Guangdong Zhou [a,b,*], Dong Lei [a,****]

[a] Department of Plastic and Reconstructive Surgery, Department of Cardiology, Shanghai Key Lab of Tissue Engineering, Shanghai 9th People's Hospital, Shanghai Jiao Tong University School of Medicine, Shanghai, 200011, PR China
[b] Research Institute of Plastic Surgery, Shandong Second Medical University, Weifang, Shandong, 261053, PR China

ARTICLE INFO

Keywords:
Underwater self-healing
Dynamic bonds
Bioelastomer
High-tension wounds
Resveratrol

ABSTRACT

The biomedical application of self-healing materials in wet or (under)water environments is quite challenging because the insulation and dissociation effects of water molecules significantly reduce the reconstruction of material–interface interactions. Rapid closure with uniform tension of high-tension wounds is often difficult, leading to further deterioration and scarring. Herein, a new type of thermosetting water-resistant self-healing bioelastomer (WRSHE) was designed by synergistically incorporating a stable polyglycerol sebacate (PGS) covalent crosslinking network and triple hybrid dynamic networks consisting of reversible disulfide metathesis (SS), and dimethylglyoxime urethane (Dou) and hydrogen bonds. And a resveratrol-loaded WRSHE (Res@WRSHE) was developed by a swelling, absorption, and crosslinked network locking strategy. WRSHEs exhibited skin-like mechanical properties in terms of nonlinear modulus behavior, biomimetic softness, high stretchability, and good elasticity, and they also achieved ultrafast and highly efficient self-healing in various liquid environments. For wound-healing applications of high-tension full-thickness skin defects, the convenient surface assembly by self-healing of WRSHEs provides uniform contraction stress to facilitate tight closure. Moreover, Res@WRSHEs gradually release resveratrol, which helps inflammatory response reduction, promotes blood vessel regeneration, and accelerates wound repair.

1. Introduction

Skin damage is one of the most common physical injuries throughout human history. The healing process of skin wounds involves various stages, including hemostasis, inflammation, proliferation, and remodeling [1,2]. However, severe skin defects pose a challenge because they cannot be closed promptly due to the high tension of the wound. These wounds become highly susceptible to microbial attacks, leading to non-healing [3–5]. Clinical treatments for high-tension wound involve reconnection of the injured tissues and closure of the defect area in order to stop bleeding, prevent leakage, and ultimately restore tissue structure and function [6]. At present, skin closure techniques including sutures, staples, tissue adhesives, and wound staplers are commonly used in clinical practice to achieve these goals [7]. While these materials have greatly improved wound and surgical care in many settings, they are often unsuitable in certain situations. Sutures and staples can be used to reduce tension on the surgical wound and to valgus the wound edge [8]. Although wound closure with these is safe and effective, it requires specialized instruments, is time consuming, operator dependent, and requires a subsequent visit for suture removal. If the closure is too tight or left in for an excessive amount of time, strangulation of tissue and suture tracks may occur [9]. Tissue adhesives provide an attractive tool kit for surgical interventions, as they can provide mechanical support and hemostatic capacity while sealing the wound site and preventing

Peer review under responsibility of KeAi Communications Co., Ltd.
* Corresponding authors.
** Corresponding author.
*** Corresponding authors.
**** Corresponding author.
E-mail addresses: doctorwangj@qq.com (J. Wang), jfzhang_dr@163.com (J. Zhang), guangdongzhou@126.com (G. Zhou), leidongjesse@qq.com (D. Lei).
[1] These authors contributed equally: Jinyi Huang, Hongying Chen, Zenghui Jia.

https://doi.org/10.1016/j.bioactmat.2024.04.009
Received 29 November 2023; Received in revised form 9 April 2024; Accepted 9 April 2024

leakage [6]. However, tissue adhesives are mostly high molecular compounds, and their composition causes a certain host immune response. In addition, differences in chemical and mechanical properties between tissue types emphasize the importance of the specificity of adhesives to the target tissue and physiological environment. A variety of wound staplers, such as ClozeX [10] and Topclosure® 3S System [11] can reduce wound tension and promote closure. However, they have the disadvantages of exposing the wound and requiring additional gauze coverage, and do not provide favorable physiological conditions to promote wound healing Therefore, an ideal wound closure material is desired. This material should possess skin-like mechanical properties and have the ability to cover exposed tissues, anti-inflammatory ability, and convenient usage to promote wound healing across multiple stages.

Recently, self-healing materials have attracted increasing attention because of their ability to autonomously repair and restore their original state after damage, similar to skin tissue [12–14]. Self-healing materials are usually constructed by noncovalent interactions and dynamic covalent bonds, including hydrogen bonds [15,16], metal coordination bonds [17,18], π–π interactions [19], ester exchange reactions [20,21], disulfide bonds [22,23], oxime amino ester bonds [24,25], etc. However, the underwater self-healing performance of these materials is significantly diminished because of the insulating effect of water molecules and their dissociating effect on weak interaction forces, such as hydrogen and ionic bonding [26]. Some hydrogel materials have underwater self-healing properties, because the hydrophilic groups on their surfaces can generate new interfacial bonding in the water environment [27,28]. However, for a large number of other non-hydrogel self-healing materials, such as polyester and polyurethane polymers, it is still difficult to form rapid and stable molecular combination under water. Moreover, Hydrogel materials contain a lot of water, which leads to a series of restrictions, including the incompatibility between the fast self-healing property and enough mechanical strength, easy dehydration and drying in body surface application, and difficulty in loading fat-soluble drugs [29]. These key challenges greatly limit the application of self-healing materials in aqueous environments such as bioengineering and clinical medicine.

In recent years, considerable research has focused on improving underwater self-healing performance through multiple dynamic bonding mechanisms. Guo et al. incorporated disulfide bonds, strongly crosslinked h-bonds, and weakly crosslinked h-bonds into the polydimethylsiloxane polymer backbone to obtain underwater high-tensile properties and rapid autonomous self-healing ability [30]. However, these approaches focused on promoting molecular chain motion and dynamic restructuring to improve self-healing efficiency, which led to unsatisfactory mechanical properties such as insufficient strength and poor elasticity. In addition, these self-healing materials lack biocompatibility and degradability, making them unsuitable for biomedical applications [31–33]. Since most biomedical applications involve liquid or wet environments such as blood and tissue fluids, self-healing biomaterials that possess a desirable combination of properties, including good biocompatibility, biomimetic mechanical properties, and underwater self-healing capabilities, to meet the requirements of biomedical applications, are desired.

Resveratrol, a lipid-soluble small-molecule drug, has gained significant scientific attention because of its biological activities, such as antioxidant, anti-inflammatory, and proangiogenic properties [34,35]. The tissue regeneration process after injury involves four phases: hemostasis, inflammation, proliferation, and remodeling. The proliferative phase, which begins shortly after the injury, encompasses crucial healing processes such as angiogenesis, collagen deposition, granulation tissue formation, and epithelialization [2]. Given that inflammation, oxidative stress, and impaired wound bed perfusion are the key factors that delay wound healing, resveratrol, with its antioxidant properties, holds promise as a supportive therapeutic approach [36,37]. According to numerous studies, it interacts with the healing cascade on multiple levels and has been found to accelerate wound healing [38–40]. Resveratrol influences wound tissue regeneration and revascularization by modulating the expression of vascular endothelial growth factor to promote regeneration and inhibit the expression of proinflammatory factors such as tumor necrosis factor-α (TNF-α). In addition, Yang et al. developed a novel pH-responsive cellulose nanofiber (CNF)-reinforced PVA/borax hydrogel that incorporated resveratrol-grafted CNFs with natural antibiotic properties [41]. In vitro and in vivo experiments, this hydrogel exhibited strong antibacterial and antioxidant properties, indicating its potential for antimicrobial effects, skin tissue regeneration, and wound repair. However, these drug-loaded materials can only improve the wound environment, and rapid wound reduction is difficult to achieve.

In this study, we designed and developed a new thermosetting PGS–SS–Dou WRSHE by integrating polyglycerol sebacate (PGS), disulfide metathesis (SS), and dimethylglyoxime urethane (Dou) units to provide stable covalent crosslinking networks and triple dynamic networks consisting of reversible disulfide, Dou, and hydrogen bonds (Fig. 1A and B). By using the swelling strategy, resveratrol was effectively loaded into WRSHEs to generate Res@WRSHEs (Fig. 1C). WRSHEs exhibit desirable properties, including skin-like mechanical properties, high toughness, high stretchability, superior elasticity, fatigue durability, water resistance, good biocompatibility, and ultrafast underwater self-healing. By taking advantage of the self-healing property, a novel and simple treatment was designed to provide rapid wound contraction for efficient healing of high-tension wounds. Compared with sterile gauze, sutures, and WRSHEs, Res@WRSHEs showed superior wound closure and healing ability. Notably, WRSHEs significantly promoted the healing of high-tension full-thickness skin wounds by regulating inflammation, accelerating collagen deposition, promoting granulation tissue formation, and enhancing vascularization (Fig. 1D). These characteristics make them promising biomaterials for clinical wound healing.

2. Materials and methods

2.1. Materials and animals

Sebacic acid (99%) and glycerol (≥99.9%) was purchased from J&K Scientific. Polytetramethylene ether glycol (PTMEG, Mn = ~2000 g mol^{-1}), dimethyl-glyoxime (DMG, 98%), Bis(4-hydroxyphenyl) disulfide, isophorone diisocyanate (IPDI, 99%), dibutyltin dilaurate (DBTDL, 95%) were purchased from Aladdin. Tetrahydrofuran (THF, ≥99.0%) and alcohol (75%) were purchased from Macklin (Shanghai Macklin Biochemical Co, Ltd.). Resveratrol (≥98.0%) was purchased from Solarbio. Lipase (≥100000U/g, from Thermophila sparsiformis) was purchased from Aladdin. Phosphate-buffered saline (PBS) was purchased from Shanghai YuanYe Biotechnology. All reagents were used as received without further purification unless otherwise noted. Sprague-Dawley male rats were purchased from Shanghai Yunde Biotechnology Co., LTD. All protocols for experimental in animals were approved by the Animal Care and Experimental Committee of Shanghai Jiao Tong University School of Medicine (SH9H-2021-A752-SB).

2.2. Synthesis of WRSHE

PGS prepolymer was synthesized by polymerization of sebacic acid and glycerol, as previously reported [42,43]. PGS prepolymer (2.5 g) was dissolved in 10 mL THF. PTMEG (4 g, 2 mmol), DMG (0.116 g, 1 mmol), Bis (4 hydroxyphenyl) Disulfide (0.25 g, 1 mmol) were dissolved in 10 mL of THF in a glass vessel equipped with a magnetic stirrer at 50 °C for 10 min. IPDI (0.944 g, 4.25 mmol) was added to the reaction mixture and then DBTDL was added to the reaction mixture immediately. The mixture reacted at 50 °C for 4 h. Then, 1 mL PGS solution (0.25 g, 0.05 mmol) was added to the mixture in ice bath environment for uniform mixing. Then, the reaction mixture was poured into a polytetrafluoroethylene mold at 90 °C, and then evaporate the solvent

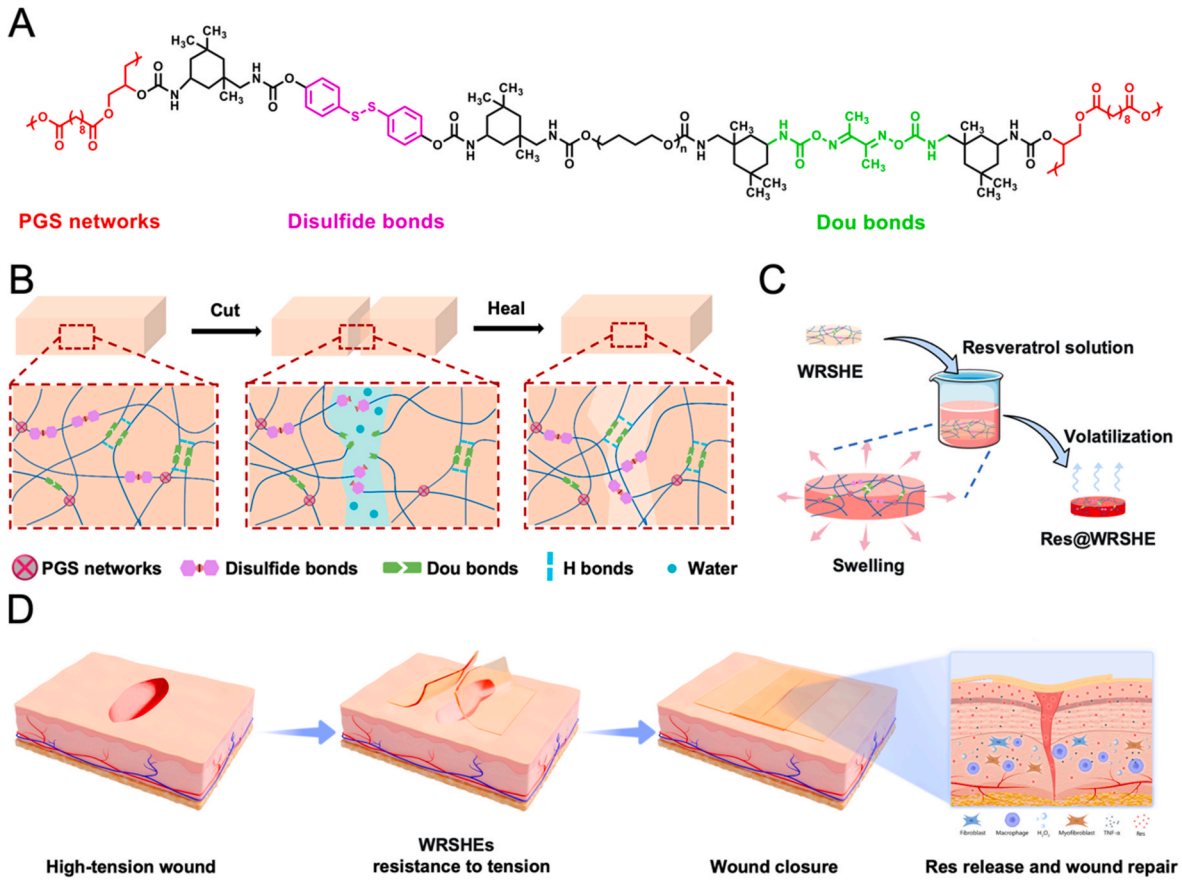

Fig. 1. Pattern diagram of chemical structural formula, self-healing mechanism, drug loading, and wound repair application of WRSHEs. (A) Chemical structure of PGS–SS–Dou WRSHE. (B) The synergistic interaction of hybrid dynamic bonds contributes to the underwater self-healing capability of WRSHEs. (C) Resveratrol penetrated and loaded in swollen and shrunken PGS–SS–Dou WRSHE crosslinking networks to generate Res@WRSHEs. (D) Application of WRSHEs in promoting contraction and healing of high-tension wounds.

under vacuum at 90 °C for 10 min. Then, the reaction mixture further cured with vacuum at 70 °C for another 12 h to produce WRSHE.

2.3. Swelling properties of WRSHE and preparation of Res@WRSHE

Swelling ratio of WRSHE in different solvents. WRSHE (diameter 5 mm) were immersed for 30 min in different liquids (water, ethanol, THF). Measuring the diameter and height before and after swelling completely to figure out the initial volume and maximum swelling volume (n = 4), which were recorded as V_i and V_m. Swelling ratio = $V_m/V_i \times 100\%$.

Preparation of Res@WRSHE. Resveratrol of 10 mg was completely dissolved in 10 ml THF. WRSHEs were immersed and swollen in resveratrol solution. The swollen WRSHEs were placed on polytetrafluoroethylene plate in the ventilated environment for 3 h to evaporate the THF.

Load and release simulations. Drug loading was simulated with red dye instead of resveratrol using the same method. And they were put into water, ethanol and THF to simulate drug release. At 1, 3, and 5 min of the release process, ethanol and THF liquids were obtained to measure the absorbance value and make a simulated sustained release curve of small molecule dye.

2.4. Characterization of WRSHE and Res@WRSHE

ATR-FTIR spectra. Attenuated total reflectance Fourier transform infra-red (ATR-FTIR) spectra was recorded on a Thermo Scientific Nicolet iS20 spectrometer.

DSC test. Differential scanning calorimetry (DSC) was performed on a Mettler DSC3. Samples were heated from −20 to 80 °C under a nitrogen atmosphere, and an additional cooling to −20 °C was added at a rate of 10 °C min^{-1}.

Water contact angle. The air-water contact angles of the samples were measured with a water contact angle instrument (Chengde Dingsheng JY-82C video contact Angle tester) at room temperature.

Resveratrol release of Res@WRSHE in vitro. The enzymatic degradation of Res@WRSHE was evaluated by using lipase from Thermophila sparsiformis. First, Res@WRSHE (0.5 mm × 10 mm × 10 mm) were immersed in 10 ml lipase/PBS solution (2000 U/ml) at 37 °C for degradation experiments. The degraded Res@WRSHE (n = 4) were taken out at the time points (1 day, 3 days, 5 days, 7 days, 9 days, 11 days, 13 days, 15 days). The solutions after degradation of each Res@WRSHE were collected. A multifunctional enzyme spectrometer (SpectraMax i3x) was used to determine the content of resveratrol in the degraded solution released from Res@WRSHE at each time point.

Mechanical properties. Tensile tests were performed on a mechanical testing machine (Instron-5542). Rectangular strips (0.5 mm × 3 mm × 20 mm) cut from large sheets were used. The tensile rates of the uniaxial tensile and cyclic tensile tests were 10 and 50 mm min^{-1}, respectively. The tensile strength was the maximum value determined from the stress–strain curve. Four specimens were tested and averaged for each sample.

2.5. Self-healing performance of WRSHE and Res@WRSHE

Restoration of the mechanical properties was assessed by splicing the two individual cut specimens at room temperature. The WRSHEs were cut into two pieces (0.5 mm × 3 mm × 10 mm) that were subsequently pressed together for healing under different conditions, including

ambient, water, ethanol and blood. The self-healing overlap length was 5 mm. Tensile tests were performed on a mechanical testing machine (Instron-5542) at different self-healing time points. The tensile rate of the uniaxial tensile was 10 mm min^{-1}.

SEM. WRSHE and Res@WRSHE were sputtered with gold and then observed in sectional view at different magnifications using Field Emission Scanning Electron Microscopy (NeoScope, JCM-5000) with an accelerating voltage of 5 kV.

2.6. Evaluation of WRSHE and Res@WRSHE biocompatibility

Cytotoxicity tests. The Cell Counting Kit-8 (CCK-8) (Dojindo, Japan) was used as previously reported to verify the biocompatibility of materials on the days of 1, 3, 7 of post-seeding respectively. Briefly, 10 μL of CCK-8 was added to the wells contained with 100 μL of MEM culture medium (11095-080, Gibco, ThermoFisher) and incubated at 37 °C for 45 min prior to measuring the absorbance values at 450 nm via spectrophotometer. Cell proliferation rate was calculated following the instructions of product manual.

Cell viability. Before live/dead cell staining (04511, sigma-aldrich), the cell slides were put on the bottom of 24-well plates and seeded with rat fibroblast cell prior to co-culture with materials. On the days of 1, 3, 7 of post-seeding, the staining was performed respectively according to manual instructions of kit and the stained cell slides were imaged under microscope (bx51; Olympus, Shinjuku, Tokyo, Japan).

Hemolytic Activity. The erythrocytes were collected by centrifugation (at 1000 rpm) from the rat's blood for 10 min. The obtained erythrocytes were washed three times with PBS buffer and further diluted to a final concentration of 5% (v/v) by PBS. Erythrocytes suspension (500 μL) and leaching liquid (500 μL) of the WRSHE, Res@WRSHE or PCL (reference material) were added to a 24-well clear plate, gently mixed by pipetting, and then shaken under100 rpm in an incubator at 37 °C for 1 h. Meanwhile, 0.1% Triton X-100 and PBS buffer were used as the positive control and the negative control, respectively. After that, the plate well contents were centrifuged at 1000 rpm for 10 min and the supernatant (100 μL) was then introduced into a new 96-well clear plate. The absorbance of the solution was read at 540 nm by a microplate reader (SpectraMax i3x). The hemolysis percentage was calculated from the relation:

Hemolysis (%) $= \frac{Ap-Ab}{At-Ab} \times 100\%$, where Ap was the absorbance value of supernatant from material groups. At was the absorbance value of the Triton X-100 positive control and Ab was the absorbance value of PBS.

In vivo biocompatibility. Subcutaneous implantation of samples in rats was used to evaluate the in vivo biocompatibility of WRSHE and Res@WRSHE. Sprague- Dawley male rats were divided into three groups (PCL used as the control). The rats were initially anesthetized by using an intraperitoneal injection of 1% pentobarbital sodium (100 mg/kg) and the dorsum was shaved and cleaned with 2% iodine prior to the procedure. Then, sterilized samples were implanted into the subcutaneous pocket. At each predetermined time point (14 and 28 days), the rats were killed and the implants with surrounding tissues were harvested. The specimens were fixed with 4% paraformaldehyde for 48 h, dehydrated with a grade series of ethanol, embedded in paraffin, and cut into slices. The slices were stained with hematoxylin and eosin (H&E) for further analysis. Paraffin sections were needed for immunostaining using primary antibodies of Ly6G (1:100, ab25377, Abcam) and F4/80 (1:100, ab90247, Abcam) to image the inflammation response. All stained slides were imaged under the automatic microscope.

2.7. Tissue adhesion of WRSHEs

The adhesive ability of WRSHEs to the host tissue was conducted by using fresh rat skin. Briefly, skin tissue and WRSHEs were cut into 20 mm × 3 mm rectangles. The WRSHE was bonded to the skin by applying polyacrylate medical pressure sensitive adhesive to its surface. The adhesive area was 5 mm × 3 mm. In the uniaxial tensile test, a lap shear test was performed at a tensile rate of 10 mm min^{-1} to test the adhesion properties.

2.8. Application of WRSHEs for wound healing

First, all rats were randomly divided into four groups, which included the sterile gauze, suture, WRSHE and Res@WRSHE, and each group contained fifteen rats. All rats were acclimatized for 1 week before surgery. All surgery procedures were performed under aseptic condition. The rats were initially anesthetized by using an intraperitoneal injection of 1% pentobarbital sodium (100 mg/kg) and the dorsum was shaved and cleaned with 2% iodine prior to the procedure. According to the normal size of the skin defect model in previous studies (≈0.8 cm) [44,45], an enlarged fusiform full-thickness high-tension wound with a long axis of 1.5 cm and a short axis of 1 cm were created on the rats' dorsum. The sterile gauze group was covered with gauze, and the suture group was closed with medical sutures. We used polyacrylate medical pressure sensitive adhesive to fix the WRSHES to the normal skin around the wound, and further used the self-healing effect to provide contraction tension to achieve rapid wound closure. WRSHE and Res@WRSHE were attached to both sides of the wound with polyacrylate medical pressure sensitive adhesive, and the elastomer was pulled down to the opposite side with the same tensile force to make it self-healing, so as to facilitate wound closure. To monitor the wound healing process, wounds were recorded by photographs on day 0, 3, 7 and 14.

2.9. Histology and immunohistochemistry

In order to evaluate the epidermal regeneration and inflammation in wound area, the collected skin samples were fixed with 4% paraformaldehyde for 48 h, embedded in paraffin, and then cross sectioned to 5 μm thickness slices. Sections obtained at 3, 7, and 14 days were stained with hematoxylin-eosin and Masson's trichrome to assess regenerating structures. CD68 and TNF-α immunofluorescence staining was performed on the regenerated skin of the wound on the 3rd and 7th days to show skin inflammation. α-SMA immunofluorescence staining was performed on the regenerated skin of the wound on the 7th and 14th days to show skin angiogenesis. The nuclei were stained with DAPI containing mounting solution. The images were further analyzed to evaluate regenerated tissue percentage by ImageJ software.

2.10. Statistical analysis

Data were analyzed with GraphPad Prism 8 software. All values were reported as a mean ± standard deviation. The data were evaluated using single-factor analysis of variance (one-way-ANOVA) and Tukey's test for simultaneous paired comparisons if conditions of normality and equal variance were met. $^{*}p < 0.05$ were considered significant.

3. Results and discussion

3.1. Synthesis and characterization of WRSHEs

The molecular structure and schematic of PGS–SS–Dou WRSHE are shown in Fig. 1A and B. WRSHEs were readily synthesized via one-pot polycondensation of polytetramethylene ether glycol, dimethylglyoxime, bis (4-hydroxyphenyl) disulfide, and isophorone diisocyanate (IPDI), followed by chemical crosslinking with a PGS prepolymer. PGS was employed as the crosslinking point because it led to a more flexible polymeric chain and enhanced the mechanical properties. In addition, PGS is biodegradable, biocompatible, and widely used as an ideal bioelastomer material for tissue engineering and regenerative medicine [42,43]. Because of the presence of flexible crosslinking networks, WRSHEs become a thermosetting material that significantly swells in organic solvents. WRSHEs were tested in water, alcohol, and THF

solvents. Macroscopic (Fig. 2A) and quantitative (Fig. 2C) analyses revealed that the highest swelling rate of WRSHEs was observed in THF, reaching 2000%, followed by 550% in alcohol and 125% in water. Using the large volume and rapid reversible swelling characteristics of WRSHEs, a new strategy of super swelling–absorption modification and crosslinked network locking was proposed to fabricate drug-loaded Res@WRSHEs. Small-molecule red dye was used as a substitute for resveratrol for visual display to simulate drug loading and release (Fig. 2B). After the solvent had completely evaporated, the dye was adsorbed and locked in molecular networks, and the WRSHE returned to its original shape. When placed into the solvents, the WRSHE swelled, and the dye was released. In THF and ethanol solvents, the dye release rates within 5 min were 82.24 ± 12.66% and 26.23 ± 2.22%, respectively. Due to the higher swelling rate of WRSHE in THF, the release rate was faster in THF than in ethanol (Figure S1A, B). This confirms that resveratrol can be conveniently and stably loaded into WRSHEs through a reversible swelling process and can avoid the reaction between the hydroxyl groups of resveratrol and IPDI, leading to drug inactivation.

Attenuated total reflectance-Fourier transform infrared spectroscopy spectroscopy was performed to confirm the molecular structure (Fig. 2D). The peaks observed at 3315 and 1716 cm^{-1} in WRSHEs corresponded to the N–H and C═O bonds in the carbamate unit, respectively, indicating the successful formation of an ethyl carbamate group. The presence of a negligible peak at 2264 cm^{-1}, corresponding to the N═C═O group, suggests that the monomeric IPDI has undergone a complete reaction. In the Res@ WRSHE group, the peaks at 1539 and 959 cm^{-1} represented the C═C bonds in resveratrol, indicating successful drug loading of resveratrol. The DSC curves of both the WRSHE and Res@WRSHE groups did not exhibit any crystallization or melting peaks within −20 °C to 80 °C (Fig. 2E). The water contact angles revealed that both the WRSHE and Res@WRSHE groups have obvious hydrophobicity, which prevents water molecules from spreading on the surface of the material (Fig. 2F). Res@WRSHE exhibited lipase catalyzed degradation properties *in vitro*. SEM images of degraded Res@WRSHE at different time points showed porous surface resulted by etching degradation (Figure S2A). Besides, with the degradation of Res@WRSHE, resveratrol was gradually released from Res@WRSHE (Figure S2B). At day 15, the cumulative release of resveratrol reached 30%. It was conducive for sustained release of resveratrol under the action of lipase in vivo and further exerted biological activity, indicating a broad application potential in drug delivery.

3.2. Skin-like mechanical properties of WRSHEs

To investigate the mechanical behavior of WRSHEs and their potential mechanisms and to assess the effect of adding resveratrol on the mechanical properties of WRSHEs, uniaxial tensile tests were conducted on PGS–SS–Dou WRSHEs and Res@WRSHEs. Both WRSHEs and Res@WRSHEs showed nonlinear stress–strain curves and exhibited similar skin-like mechanical behaviors such as high strength, toughness, stretchability, and biomimetic stiffness (Fig. 2G). No significant difference was found between the two groups. The stress–strain curves were divided into three regions depending on the range of deformation: the linear region in the low strain region (region i), nonlinear region in the middle strain region (region ii), and linear region in the high strain region (region iii). The tensile strength of WRSHEs was 1.536 ± 0.22 MPa (Fig. 2H), and the elongation at break was 793 ± 19.6 % (Fig. 2I). The tensile strength of Res@WRSHEs was 1.495 ± 0.28 MPa, and the elongation at break was 846 ± 66.6%. The elastic modulus of each region in the two groups was statistically analyzed (Fig. 2J). In region i (strain 0–10 %), the WRSHE and Res@WRSHE groups exhibited higher elastic moduli of 0.691 ± 0.07 MPa and 0.628 ± 0.09 MPa, respectively, which was contributed by the dynamic crosslinking networks. The initial elastic modulus of WRSHEs in region i was extremely similar to that of the skin (0.42–0.75 MPa) [46,47]. With increasing strain, the sacrifice hydrogen, disulfide, and Dou bonds dissociated to effectively dissipate mechanical energy, resulting in a smaller slope of the stress–strain curve in region ii (strain 10–500%) than in region i. In region iii (strain >500%), the dissociation of dynamic sacrifice bonds might reach saturation, and the stable PGS covalent crosslinking network contributed significantly to the resistance of the applied strain. Consequently, the modulus of region iii increased rapidly compared with that of region ii. This unique nonlinear stress–strain behavior of WRSHEs with self-stiffening characteristics during stretching is similar to that of the human skin, which is suitable for skin wound repair and provides better comfort.

Cyclic tensile tests at different strains were performed to evaluate the stretching properties and further demonstrate the aforementioned mechanism. First, continuous cyclic stretching of the WRSHEs was performed by gradually increasing the strain (Fig. 2K and L). At first cycle within lower strain (100%), most of the dynamic networks were maintained to a higher modulus and stress resistance. However, as weaker dynamic bonds dissociate, some networks are opened, reducing their ability to resist external stress and gradually decreasing the stiffness. With an increase in strain (≥200%), the WRSHE group exhibited observable residual strain and an attenuated modulus, which is due to the reformation of partially ruptured dynamic bonds at new sites. In the subsequent continuous cyclic stretching, the already dissociated dynamic bonds did not form new combination in time, resulting in a decrease in stiffness compared to the previous cycle.

Next, cyclic tensile tests were subsequently performed with a repetitive strain of 500%, without a waiting period (Fig. 2M). The obvious hysteresis loops in the first cycle indicated that part of the applied mechanical energy during the stretching process was successfully dissipated by the WRSHEs. During the stretching process, energy dissipation was mainly achieved through the dissociation of dynamic bonds. As the number of cyclic stretching increases, the dynamic networks gradually opened up and the energy dissipation effect gradually decreased. As the number of cycles increased, hysteresis was reduced, and the cyclic stress–strain curves gradually tended to be consistent, showing good elasticity and fatigue resistance. This could be attributed to the elasticity of the stable PGS covalent crosslinking network and the achievement of a balance between the dissociation and reorganization of dynamic bonds during continuous cyclic stretching. Notably, the 11th cycle curves of both the WRSHE and Res@WRSHE groups were similar to their first curves within a short waiting time of 5 min at 37 °C. The difference was not statistically significant (Fig. 2N–P). The recovery process showed competition between the contractile force of the elastic PGS covalent network pulling against temporary hydrogen, Dou, and disulfide bonds. The stronger elastic contraction of the stable PGS network efficiently dissociated the reformed dynamic bonds and resulted in the rapid recovery of the molecular structure, morphology, and mechanical properties. The robust restoration and excellent resilience of WRSHEs are favorable for practical wound healing applications to provide effective uniform mechanical support.

3.3. Underwater self-healing properties and biocompatibility of WRSHEs

For biomedical applications, particularly skin wound healing, the applied materials must have efficient self-healing properties in various wet and/or (under) water environments such as blood, tissue fluid, sweat, and ethanol used for disinfection. In the past decade, much effort has been made to develop autonomous self-healing materials under ambient conditions [12,15,19]. However, only a few materials achieved autonomous self-healing under underwater conditions [30]. Most of these materials aim to promote molecular motion to improve self-healing efficiency but lead to a decrease in mechanical properties. Therefore, achieving highly efficient underwater self-healing of materials while retaining their strong and tough mechanical properties remains a key challenge. Furthermore, most self-healing materials are not developed as biomaterials for biomedical applications, resulting in biocompatibility and biodegradability problems. To the best of our

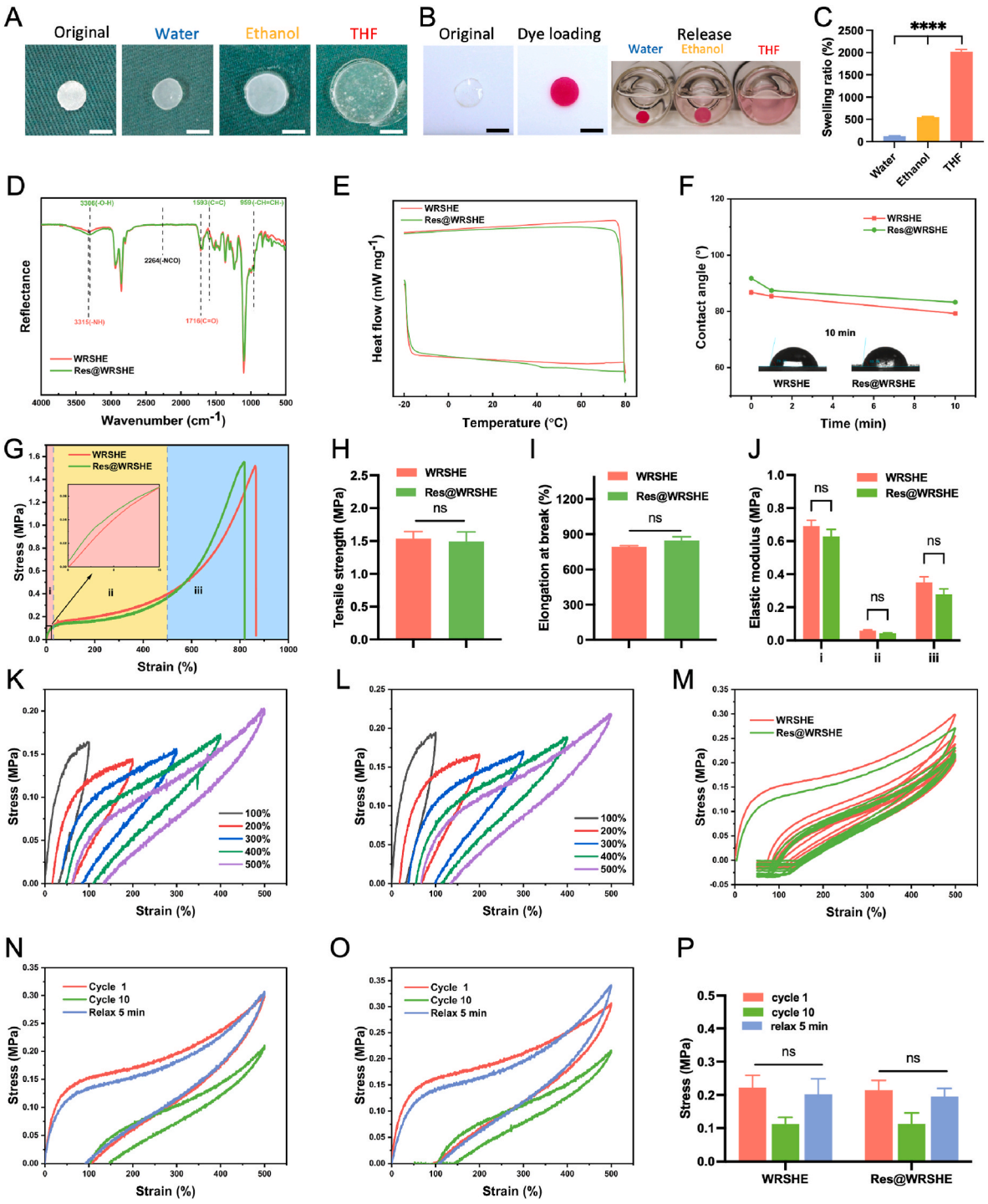

Fig. 2. Reversible swelling, resveratrol loading, structural analysis, water resistance, and skin-like mechanical properties of WRSHEs. (A) Photographs of PGS–SS–Dou WRSHEs and the equilibrium swelling states in different solvents. Scale bar = 5 mm. (B) Small-molecule red dye was loaded into WRSHEs and then released in different solvents. Scale bar = 5 mm. (C) Swelling rate of WRSHEs. (D) ATR-FTIR spectra of WRSHEs and Res@WRSHEs. (E) DSC curves of WRSHEs and Res@WRSHEs. (F) Dynamic water contact angle measurements of WRSHEs and Res@WRSHEs. (G) Typical tensile stress–strain curves of WRSHEs and Res@WRSHEs. With the dependence of stress on strain, the curves can be divided into three regions depending on the range of strain. The enlarged image shows the deformation range of 0–10%. (H–K) Statistical analysis of tensile strength (H), maximum elongation (I), and elastic modulus in three regions (J) of WRSHEs and Res@WRSHEs (n = 4). (K, L) Sequential cyclic tensile curves of WRSHEs (K) and Res@WRSHEs (L) with increasing strain without any resting period. (M) Cyclic tensile curves of WRSHEs and Res@WRSHEs at a strain of 500%. No waiting time was found between two consecutive cyclic tensile (cycles 1–10). (N, O) Repeated cyclic tensile curves of WRSHEs (N) and Res@WRSHEs (O) with a maximum strain of 500% (10 cycles). The stretched film was allowed to relax for 5 min at 37 °C before the 11th cyclic tensile test. (P) Stress of cycle 1, cycle 10, and cycle 11 (after relax 5 min) at 250% strain. (n = 4). *$p < 0.05$, ****$p < 0.0001$.

knowledge, self-healing biomaterials for biomedical applications are still in the early stages of development, and currently, no self-healing material has been reported to provide effective contraction tension for promoting wound repair. In this work, PGS–SS–Dou WRSHEs not only possessed skin-like mechanical properties but also exhibited universal self-healing capability because of their stable PGS network and dynamic disulfide, Dou, and hydrogen bonds.

The WRSHEs were cut into two pieces and subsequently pressed together for healing without any external simulation under different periods and conditions. When the two surfaces were pressed and in contact, the dynamic bonds dissociated under pressure. At this point, the free hydrogen bonds and newly dissociated bonds randomly combined with the sacrificed bonds on the other side, resulting in self-healing (Fig. 3A). The electron micrographs showed that the self-healing interface of the PGS–SS–Dou WRSHE was nearly invisible after 10 min of self-healing (Fig. 3B). After 1 min and 1 h of self-healing at room temperature, the PGS–SS–Dou WRSHE group exhibited universal self-healing properties under different liquids (water, ethanol, and blood) without fracturing after stretching (Fig. 3C and Movie S1, S2). Moreover, we compared the self-healing properties of WRSHE under different liquids (Figure S3 A-C). The mechanical properties of WRSHE remained stable after self-healing in water, ethanol and blood for 1 min. Moreover, the mechanical properties of WRSHE after self-healing for 1 h in water and blood was still similar to those for 1 min. Water molecules and physiological ions in blood have little effect on the self-healing properties of WRSHE, and the mechanical properties of WRSHE remain stable after a long time of liquid immersion. Statistical analysis showed no significant difference. However, after 1 h of self-healing of WRSHE in ethanol, elongation at break and tensile strength decreased significantly and mechanical properties decreased due to the swelling effect of ethanol.

Furthermore, the self-healing strengths of the WRSHE and Res@WRSHE groups under ambient and underwater conditions were evaluated after 1 min and 1 h of self-healing. Under ambient conditions, the mechanical curves of the WRSHE group were nearly identical after self-healing at 1 min and 1 h (Fig. 3D). The loading of resveratrol did not change the self-healing performance of the WRSHE group, and the Res@WRSHE group exhibited a stress–strain curve similar to that of the WRSHE group. The fracture strength of the WRSHE group was approximately 1 MPa, with a maximum strain exceeding 650%, and the fracture did not occur at the self-healing site (Fig. 3E and F). These results demonstrate that WRSHEs possess fast and highly efficient self-healing ability. In underwater environments, the WRSHE group still exhibited satisfactory self-healing effects because of surface hydrophobicity and hybrid dynamic bonds (Fig. 3G). Because of the dissociation of partially restructured hydrogen bonds by water molecules, the tensile properties slightly decreased with time; however, the strength and maximum strain still exceeded 0.8 MPa and 550%, respectively (Fig. 3H and I).

In addition, biocompatibility is a general requirement for all biomaterials, the safety of the WRSHEs needs to be determined prior to in vivo applications. The proliferation of fibroblasts co-cultured with WRSHEs was satisfactory. The results of cck-8 and live/dead staining showed that WRSHE and Res@WRSHE had similar cytocompatibility compared with PCL (Fig. 3J and K and Figure S4A). Furthermore, WRSHEs are in direct contact with human blood, skin, and subcutaneous tissue. Therefore, the biocompatibility of WRSHEs was evaluated in terms of hemocompatibility and host responses to implants. The hemolysis ratios were then calculated using the Triton group as the standard, and the WRSHEs group demonstrated excellent hemocompatibility with hemolysis ratios <5% (Figure S4B). Results of HE staining showed that the WRSHE and Res@WRSHE groups was surrounded by loose connective tissue, which was similar to the PCL group (Fig. 3L and Figure S5). Immunohistochemical staining of Ly6G (acute subcutaneous inflammation response) and F4/80 (chronic subcutaneous inflammation response) showed that PCL, WRSHE, and Res@WRSHE all caused mild acute and chronic inflammatory responses after subcutaneous implantation, and there was no statistically significant difference in inflammatory responses caused by the three materials (Fig. 3M and Figure S5). These results demonstrated that the WRSHE and Res@WRSHE groups exhibited comparable biocompatibility with the commonly used biomaterial PCL. The skin adhesion of materials was achieved through the use of medical pressure-sensitive adhesives at their interfaces. In the lap shear test of rat skin, WRSHEs showed sufficient and stable adhesion strength (0.362 ± 0.008 MPa) with the skin (Figure S6). Therefore, WRSHEs exhibited ultrafast and highly efficient underwater self-healing performance, resilient skin-like mechanical properties, and reliable biocompatibility, indicating potential applications in biomedical applications, particularly in promoting wound contraction and healing.

3.4. Application of WRSHEs for wound healing

Recently, some self-healing hydrogel materials have been applied in wound repair, but hydrogel was directly implanted into the wound area to achieve wound repair by tissue growth and fusion, and does not use self-healing function [44,45]. In this work, the self-healing properties of WRSHE are utilized to achieve surface assembly and provide uniform contraction stress to promote tight wound closure. To investigate the repair performance of WRSHEs on skin wounds, a high-tension full--thickness skin defect model in rats was examined. The back incisions of rats were closed using WRSHE and Res@WRSHE, which uniformly resisted the tension of the wound (Fig. 4A). Sterile gauze and sutures were used as controls. From a gross view (Fig. 4B), the transparency of WRSHEs facilitated wound management and precise anastomosis, which are crucial steps for achieving optimal healing. Moreover, the sutured wound showed an uneven closure morphology. On postoperative day 3, significant improvement and formation of sealed wounds were observed in both the WRSHE and Res@WRSHE groups. However, thick scabs and clear reconnection marks were observed in the sterile gauze and suture groups. On postoperative day 7, the WRSHEs groups showed significantly faster healing rates than the other groups, whereas the sterile gauze group still had wound gaps. On postoperative day 14, the WRSHEs groups exhibited clear signs of good wound healing without scarring. Importantly, throughout the study, the skin did not show any redness, swelling, ulceration, or other adverse symptoms upon WRSHEs removal, indicating the biological safety of WRSHEs.

Histological examination of HE staining showed (Fig. 4D) that after 3 days of treatment, the sterile gauze group exhibited delayed epithelial regeneration. In the suture group, uniform tight wound healing failed. The WRSHE and Res@WRSHE groups demonstrated superior outcomes, tight wound closure, re-epithelialization, and absence of scab formation. Inflammatory cell infiltration in varying degrees and fibroblast migration and proliferation were observed in the four groups, leading to the formation of granulation tissue. Interestingly, the Res@WRSHE group exhibited weaker inflammatory infiltration and thicker granulation tissue than the WRSHE group. The WRSHE group showed insufficient granulation tissue filling and tissue vacancy in the closed wound, which may be caused by a higher inflammatory reaction that delayed tissue healing. On postoperative day 7, histology showed that the wounds in the sterile gauze group were still filled with broad granulation tissue, and no new skin appendages appeared. In the suture group, the new epidermis was thickened and deformed (green enlarged area in the suture group on postoperative day 7), and it was also filled with new granulation tissue without new skin appendages (red enlarged area in the suture group on postoperative day 7). Epithelial thickness was considered to increase during the inflammatory and proliferative stages and decrease during the remodeling stage [48]. Interestingly, the thickness of the new epithelium in the Res@WRSHE group was close to that of normal skin, and no excessive hyperplasia or thickening was observed, indicating excellent tissue remodeling. In addition, new skin appendages (hair follicles, etc.) began to appear, and the overall regeneration morphology was better than that of the WRSHE group. On day 14, no skin appendage appeared in the repair area of the gauze

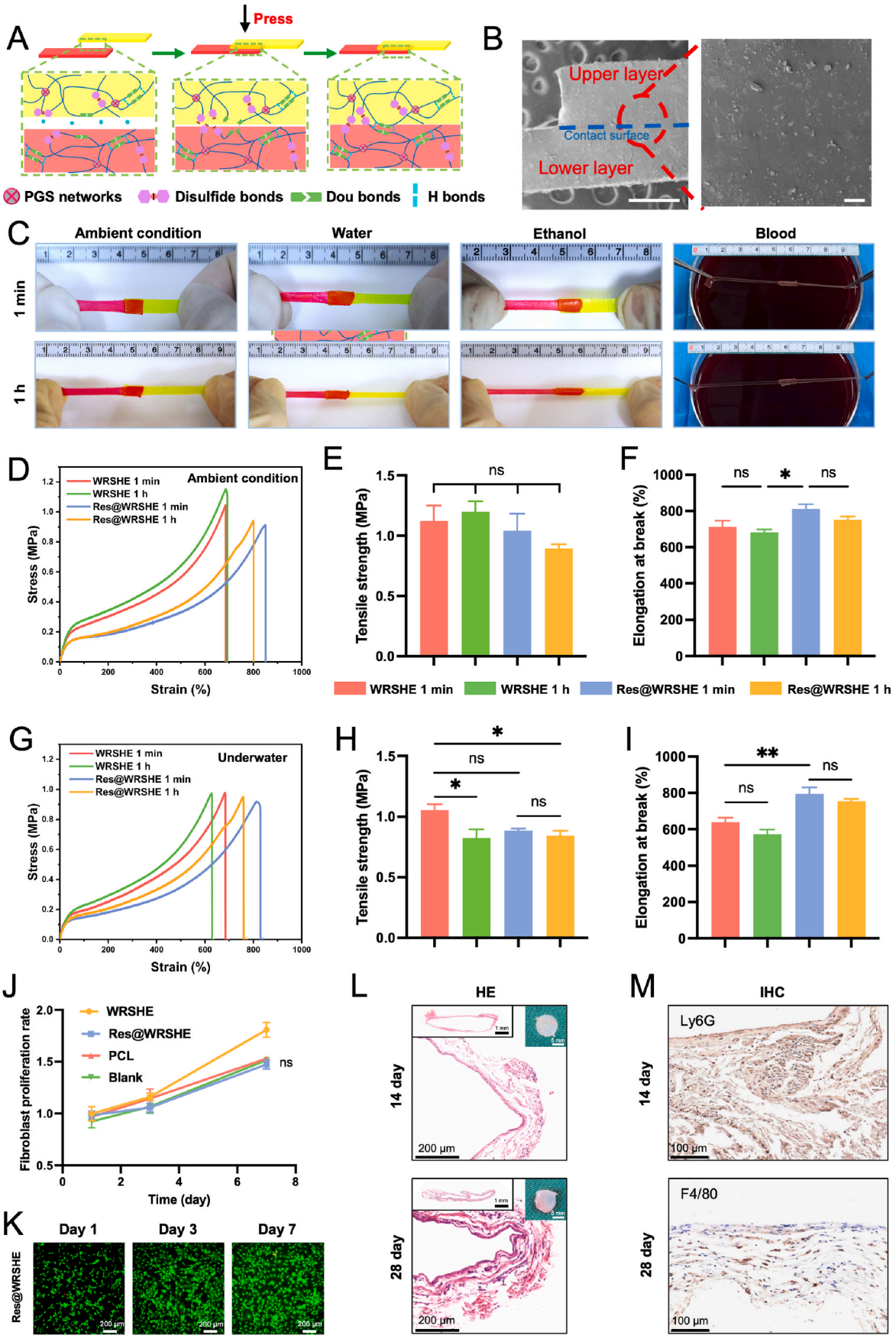

(caption on next page)

Fig. 3. Self-healing capability and biocompatibility of WRSHEs. (A) Schematic mechanism of interface self-healing underwater. (B) SEM image of the self-healing interface after 10 min under ambient conditions. Scale bar = 500 and 100 μm. (C) Cut WRSHEs colored with dyes and the contact for self-healing. Healed sample that was stretched after healing under ambient conditions and in different solvents (water, ethanol, and blood) at room temperature for 1 min and 1 h. (D–F) Mechanical properties of WRSHEs and Res@WRSHEs after 1 min and 1 h of self-healing under ambient conditions at room temperature. Stress–strain curves (D), tensile strength (E), and elongation at break (F). (G–I) Mechanical properties of WRSHEs and Res@WRSHEs after 1 min and 1 h of self-healing underwater at room temperature. Stress–strain curves (G), tensile strength (H), and elongation at break (I). n = 4. (J) Proliferation rate of rat fibroblast cell co-cultured with PCL, WRSHE, and Res@WRSHE (as a positive control) respectively on day1, day 3 and day 7 (n = 5 in each group). (K) Live and dead staining of rat fibroblast cell co-cultured with Res@WRSHE on day 1, day 3 and day 7. (L) Representative micrographs of H&E-stained sections of Res@WRSHE. (M) Representative micrographs of IHC stained (Ly6G and F4/80) sections of Res@WRSHE. n = 4. $^{*}p < 0.05$, $^{**}p < 0.01$.

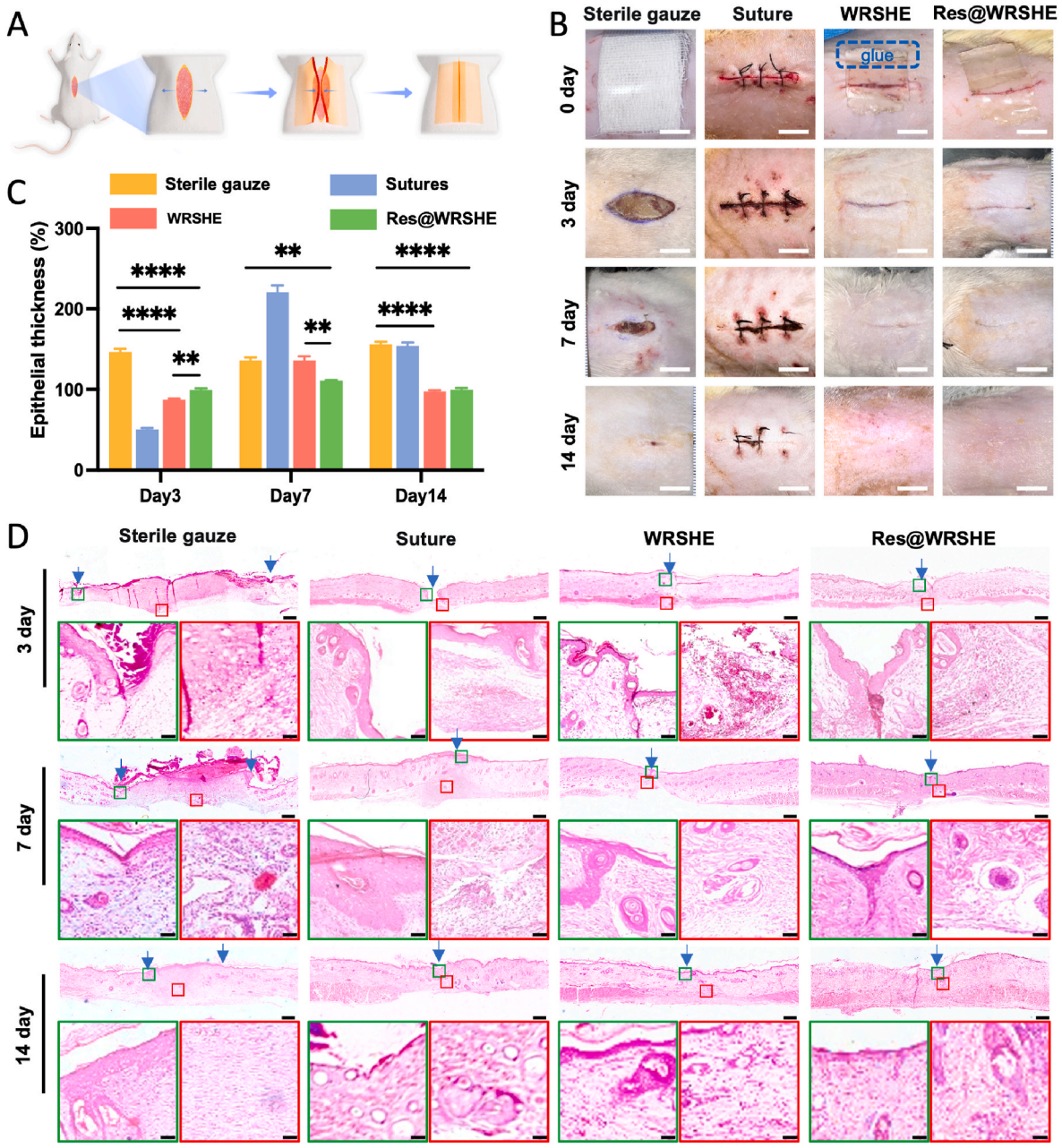

Fig. 4. Skin wound closure and healing. (A) Schematic of the surgical process. (B) Representative photographs of the wound repair process using sterile gauze, suture, WRSHE and Res@WRSHE. Scale bar = 1 cm. (C) Percentage of regenerated epithelial thickness to normal epithelial thickness. (D) HE staining of the regenerated skin wounds after sterile gauze, suture, WRSHE and Res@WRSHE treatment on postoperative days 3, 7 and 14. The blue arrow represents the incision. The green rectangle represents the junction between the incision and normal skin. The red rectangle represents the bottom of the wound. Scale bar = 500 μm; Scale bar = 50 μm (green and red rectangles). N = 4, $^{*}p < 0.05$, $^{**}p < 0.01$, $^{***}p < 0.001$, and $^{****}p < 0.0001$.

group, and the other three groups gradually transitioned from the proliferative phase to the remodeling phase. The Res@WRSHE group had near-complete regeneration of skin appendages and the largest number of hair follicles, and clearly showed mature tissue arrangement.

Masson's trichrome staining (Fig. 5A) revealed that the collagen fibers in the sterile gauze and suture groups were loosely and disorderly

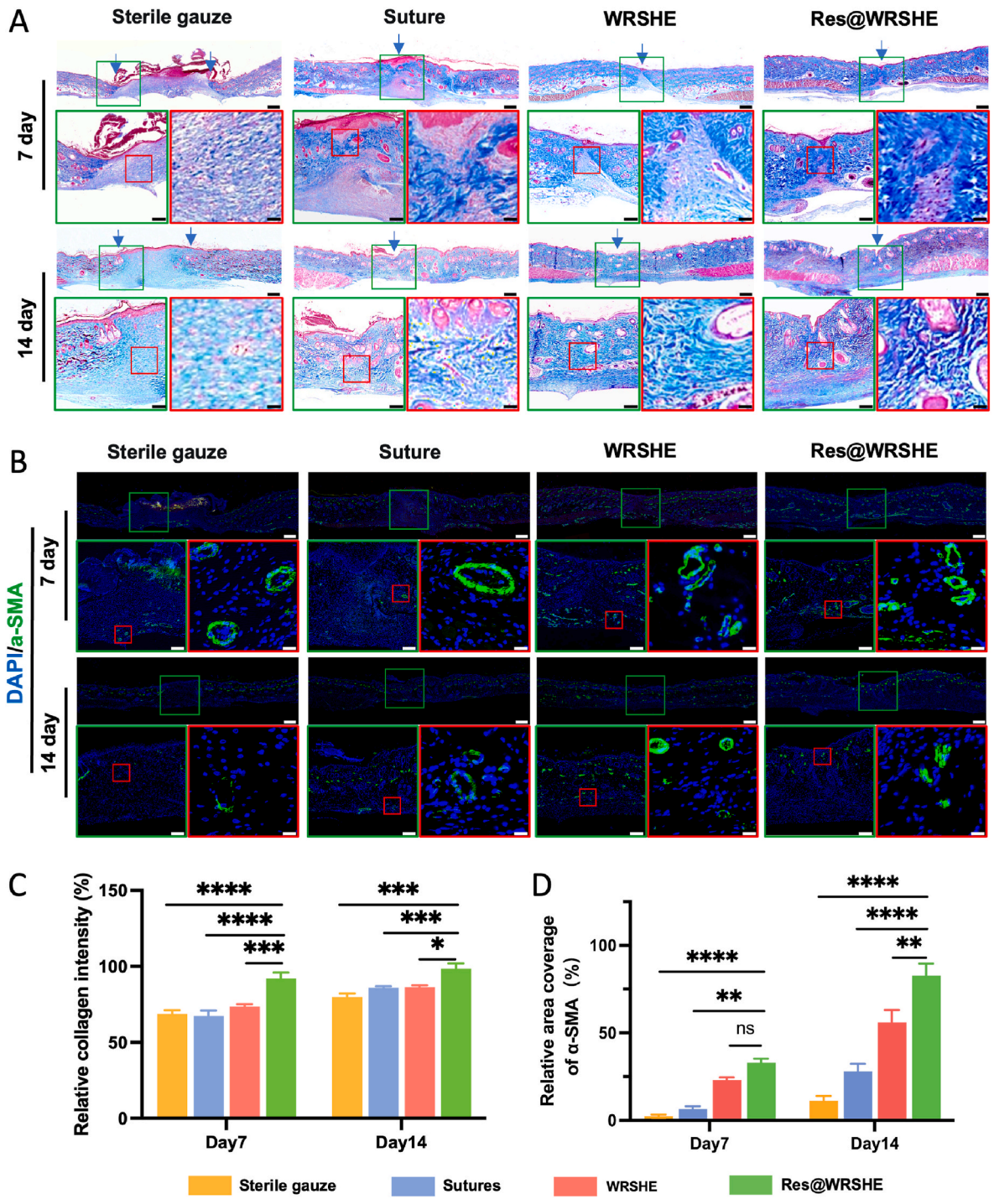

Fig. 5. Collagen deposition and vascularization during wound healing. (A) Masson staining of regenerated skin wounds after sterile gauze, suture, WRSHE and Res@WRSHE treatments on postoperative days 7 and 14. The blue arrow represents the incision. The green and red rectangles represent the magnified area. Scale bar = 500, 200 and 50 μm. (B) Representative immunofluorescence images of regenerated wound tissues labeled with α-SMA (green) on days 7 and 14. The green and red rectangles represent the magnified area. Scale bar = 500, 200 and 20 μm. (C) Quantification of collagen intensity in the image. For the data, normal skin collagen intensity was set at 100%. (D) Quantitative analysis of the relative percentage of area coverage by α-SMA. For the data, normal skin vascular content was set as 100%. n = 4, $^{*}p < 0.05$, $^{**}p < 0.01$, $^{***}p < 0.001$, and $^{****}p < 0.0001$.

arranged because of delayed wound healing. The WRSHE and Res@WRSHE groups showed rapid generation of collagen deposits at the junction site from the early stage. Notably, the Res@WRSHE group exhibited more abundant and neatly arranged collagen, appearing dark blue and having similar morphology and quality to normal skin. This finding was further supported by the quantitative analysis of the associated collagen (Fig. 5C). These promising results can be attributed to the unique behavior of Res@WRSHE, which released resveratrol at the wound, facilitating a swift transition from the inflammatory phase to the remodeling state. Vascularization of the wound area is crucial for adequate nutrition during wound healing. Immunofluorescence staining for alpha smooth muscle actin (α-SMA) in the regenerated tissue demonstrated (Fig. 5B) significantly higher α-SMA-positive staining and generation of more blood vessels with a larger diameter in the wound

area of the Res@WRSHE group on postoperative day 7. In contrast, the sterile gauze and suture groups exhibited less α-SMA-positive staining. Quantitative analysis confirmed that the Res@WRSHE group exhibited the highest degree of neovascularization on postoperative day 7 (Fig. 5D). In addition, more neovascularization was observed in the WRSHE group than in the sterile gauze and suture groups, second only to the Res@WRSHE group. This finding suggests that WRSHE alone partially accelerated the wound repair process, although the degree of neovascularization was still inferior to that in the Res@WRSHE group. On postoperative day 14, the blood vessels in the Res@WRSHE group exhibited a neat arrangement, resembling the morphology of normal skin blood vessels. In addition, the α-SMA-positive staining area accounted for 83% of that in normal skin blood vessels. Overall, the temporal trend of vascularization in the wounds of the Res@WRSHE group indicated that it enabled the wounds to transition quickly from the proliferation stage to the remodeling stage.

The vascular differentiation may be attributed to the release of resveratrol from Res@WRSHE, which plays a proangiogenic role. Numerous studies have demonstrated the perfusion-enhancing effects of resveratrol [49–51]. The proangiogenic potential of resveratrol is primarily dependent on the SIRT1-mediated deacetylation of FOXO1. Key factors in wound healing include inflammation, oxidative stress, and impaired wound bed perfusion (Fig. 6A). As a powerful antioxidant, resveratrol not only induces vascular endothelial growth, promotes wound angiogenesis, and restores wound bed blood perfusion during wound healing but also combats oxidative stress and reduces ROS levels in the wound [34,40,52]. This phenomenon improves the inflammatory response of the wound and accelerates the transition from the

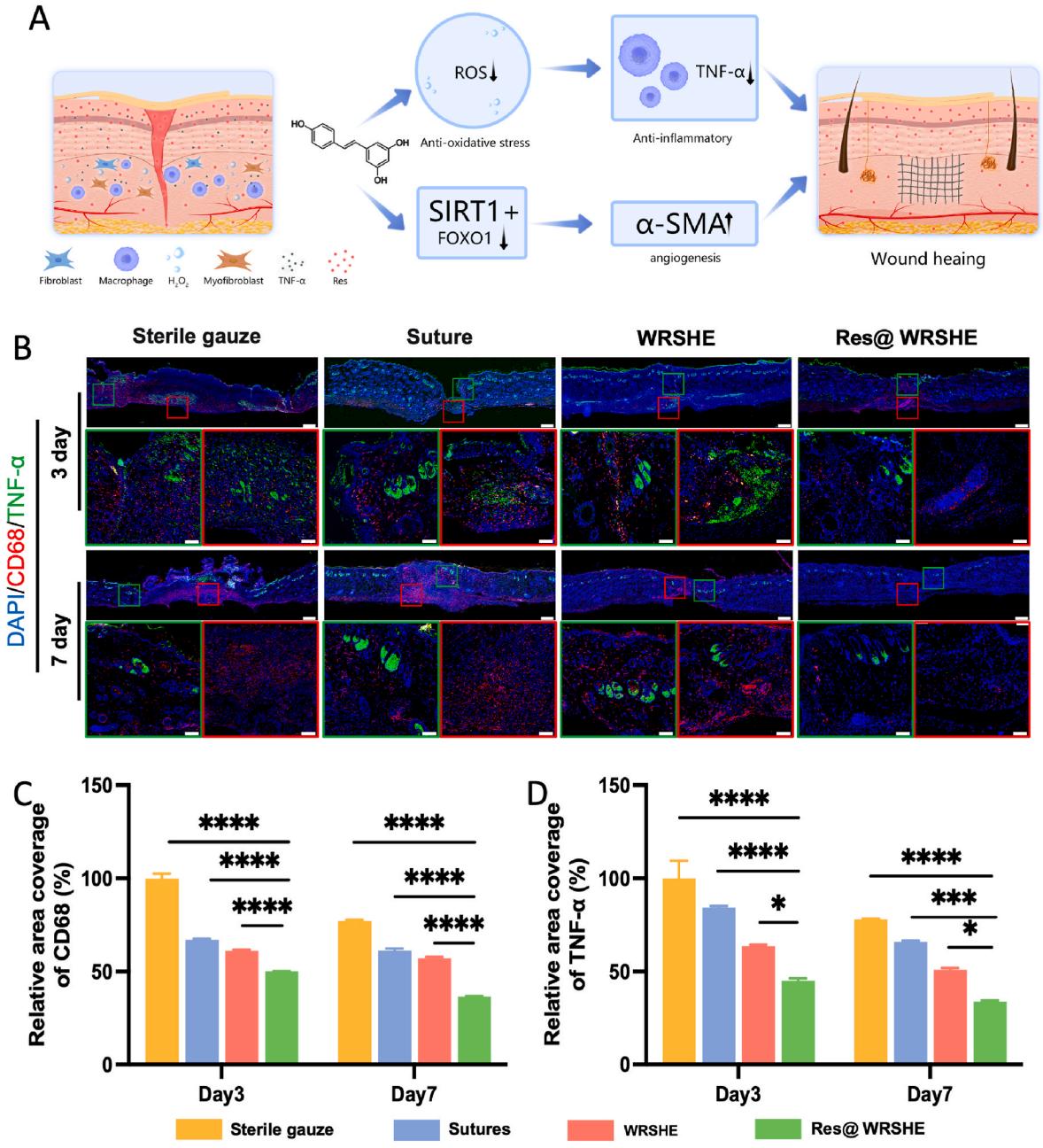

Fig. 6. Anti-inflammatory effects of Res@WRSHEs on wound healing. (A) Schematic mechanism of resveratrol to promote wound healing. (B) Representative immunofluorescence images of regenerated wound tissues labeled with TNF-α (green) and CD68 (red) on days 3 and 7. The green and red rectangles represent the magnified area. Scale bar = 500 and 50 μm. (C and D) Quantitative analysis of the relative percentage of area coverage by CD68 (C) and TNF-α (D). For the data, the sterile gauze group was set as 100%. n = 4, *$p < 0.05$, **$p < 0.01$, ***$p < 0.001$, and ****$p < 0.0001$.

inflammatory phase to the proliferative phase of wound healing. To evaluate the effectiveness of Res@WRSHEs in reducing wound inflammation, immunofluorescence analysis was performed.

In this study, CD68 and TNF-α [44,53], two typical inflammatory markers in the wound site, were selected as the evaluation criteria (Fig. 6B). On postoperative day 3, high levels of CD68 (red fluorescence) were detected in the sterile gauze, suture, and WRSHE groups, indicating an inflammatory response in the wound area. In addition, strong green fluorescence was detected in these control groups, indicating high levels of secreted TNF-α. Encouragingly, only a small amount of red and green fluorescence was detected in the Res@WRSHE group, indicating a lower degree of inflammation than in the other samples. On postoperative day 7, the fluorescence intensity decreased to some extent in all groups, with the Res@WRSHE group remaining the weakest. Quantitative analysis and fluorescent staining supported the same results (Fig. 6C and D), with the least amount of inflammatory factors and the lowest intensity of fluorescent expression in the Res@WRSHE group. These results indicate that Res@WRSHE exhibits superior anti-inflammatory properties. Therefore, Res@WRSHEs are potential wound repair materials that provide ideal wound healing ability while avoiding inflammation.

4. Conclusion

We have designed and synthesized a WRSHE that exhibits not only skin-like nonlinear mechanical properties with a biomimetic modulus (≈0.5 MPa), high stretchability (≈800%), good strength (≈1.5 MPa), and good elasticity but also universally fast self-healing capability in various liquid environments. The key to achieving these properties is the synergistic effect of stable covalent crosslinking networks of PGS and multiple dynamic bonds, including SS, reversible Dou, and hydrogen bonds. Notably, WRSHEs can generate uniform and sufficient mechanical support to resist wound tension, ensuring accurate wound closure and releasing the anti-inflammatory and angiogenic drug resveratrol to promote faster healing. In previous studies, some self-healing materials are used for wound healing, but these are hydrogels. Most self-healing hydrogels are only used as dressings for surface coverage to repair wounds and do not take advantage of the self-healing properties. To the best of our knowledge, Res@WRSHEs, as a non-hydrogel material, is the first time to use self-healing properties to form interface assembly and provide contraction stress, and combine with drug release in wound-healing applications. This work effectively utilized underwater self-healing properties as the key to address high-tension full-thickness skin defects and could inspire several new biomedical applications of self-healing materials.

Ethics approval and consent to participate

All protocols for experimental in animals were approved by the Animal Care and Experimental Committee of Shanghai Jiao Tong University School of Medicine (SH9H-2021-A752-SB).

Conflict of interest

The authors declare no competing interests.

CRediT authorship contribution statement

Jinyi Huang: Writing – original draft, Visualization, Software, Methodology, Formal analysis, Data curation, Conceptualization. **Hongying Chen:** Writing – original draft, Software, Methodology, Data curation. **Zenghui Jia:** Writing – original draft, Methodology, Data curation, Conceptualization. **Xingqi Song:** Writing – original draft, Data curation. **Sinan Wang:** Writing – original draft, Data curation. **Baoshuai Bai:** Writing – original draft, Data curation. **Jian Wang:** Writing – review & editing, Supervision, Funding acquisition. **Junfeng Zhang:** Project administration, Methodology, Investigation. **Guangdong Zhou:** Writing – review & editing, Supervision, Funding acquisition. **Dong Lei:** Validation, Resources, Project administration, Methodology, Investigation, Funding acquisition, Conceptualization.

Acknowledgements

This research was financially supported by the National Key Research and Development Program of China (2022YFA1207500), the National Key Research and Development Program of China (2022YFC2409803), Biomaterials and Regenerative Medicine Institute Cooperative Research Project of Shanghai Jiaotong University School of Medicine (2022LHA07), the National Natural Science Foundation of China (82102211), Experimental Animal Research Project of Shanghai Science and Technology Commission (No.22140901200), and Shanghai Municipal Key Clinical Specialty (shslczdzk06601).

Appendix A. Supplementary data

Supplementary data to this article can be found online at https://doi.org/10.1016/j.bioactmat.2024.04.009.

References

[1] G.C. Gurtner, S. Werner, Y. Barrandon, M.T. Longaker, Wound repair and regeneration, Nature 453 (7193) (2008) 314–321.
[2] S.A. Eming, T.A. Wynn, P. Martin, Inflammation and metabolism in tissue repair and regeneration, Science 356 (6342) (2017) 1026–1030.
[3] R.F. Diegelmann, M.C. Evans, Wound healing: an overview of acute, fibrotic and delayed healing, Front. Biosci. 9 (1) (2004) 283–289.
[4] M. Xue, C.J. Jackson, Extracellular Matrix reorganization during wound healing and its Impact on Abnormal scarring, Adv. Wound Care 4 (3) (2015) 119–136.
[5] G.M. Taboada, K. Yang, M.J.N. Pereira, S.S. Liu, Y. Hu, J.M. Karp, N. Artzi, Y. Lee, Overcoming the translational barriers of tissue adhesives, Nat. Rev. Mater. 5 (4) (2020) 310–329.
[6] S. Nam, D. Mooney, Polymeric tissue adhesives, Chem. Rev. 121 (18) (2021) 11336–11384.
[7] L. Al-Mubarak, M. Al-Haddab, Cutaneous wound closure materials: an overview and update, J. Cutan. Aesthetic Surg. 6 (4) (2013) 178.
[8] T.O. Smith, D. Sexton, C. Mann, S. Donell, Sutures versus staples for skin closure in orthopaedic surgery: meta-analysis, Br. Med. J. 340 (7749) (2010) 747.
[9] N. Annabi, Y.-N. Zhang, A. Assmann, E.S. Sani, G. Cheng, A.D. Lassaletta, A. Vegh, B. Dehghani, G.U. Ruiz-Esparza, X. Wang, S. Gangadharan, A.S. Weiss, A. Khademhosseini, Engineering a highly elastic human protein–based sealant for surgical applications, Sci. Transl. Med. 9 (410) (2017) eaai7466.
[10] F. Kuo, D. Lee, G.S. Rogers, Prospective, Randomized, Blinded study of a new wound closure film versus Cutaneous suture for surgical wound closure, Dermatol. Surg. 32 (5) (2006) 676–681.
[11] M. Topaz, N.-N. Carmel, A. Silberman, M.S. Li, Y.Z. Li, The TopClosure® 3S System, for skin stretching and a secure wound closure, Eur. J. Plast. Surg. 35 (7) (2012) 533–543.
[12] S. Bonardd, M. Nandi, J.I. Hernández García, B. Maiti, A. Abramov, D. Díaz Díaz, Self-healing polymeric soft Actuators, Chem. Rev. 123 (2) (2023) 736–810.
[13] C.E. Diesendruck, N.R. Sottos, J.S. Moore, S.R. White, Biomimetic self-healing, Angew. Chem. Int. Ed. 54 (36) (2015) 10428–10447.
[14] C.-M. Yeh, C.-H. Lin, T.-Y. Han, Y.-T. Xiao, Y.-A. Chen, H.-H. Chou, Disulfide bond and Diels–Alder reaction bond hybrid polymers with high stretchability, transparency, recyclability, and intrinsic dual healability for skin-like tactile sensing, J. Mater. Chem. A 9 (10) (2021) 6109–6116.
[15] P. Cordier, F. Tournilhac, C. Soulié-Ziakovic, L. Leibler, Self-healing and thermoreversible rubber from supramolecular assembly, Nature 451 (7181) (2008) 977–980.
[16] Y. Yanagisawa, Y. Nan, K. Okuro, T. Aida, Mechanically robust, readily repairable polymers via tailored noncovalent cross-linking, Science 359 (6371) (2018) 72–76.
[17] C.-H. Li, C. Wang, C. Keplinger, J.-L. Zuo, L. Jin, Y. Sun, P. Zheng, Y. Cao, F. Lissel, C. Linder, X.-Z. You, Z. Bao, A highly stretchable autonomous self-healing elastomer, Nat. Chem. 8 (6) (2016) 618–624.
[18] J.-C. Lai, L. Li, D.-P. Wang, M.-H. Zhang, S.-R. Mo, X. Wang, K.-Y. Zeng, C.-H. Li, Q. Jiang, X.-Z. You, J.-L. Zuo, A rigid and healable polymer cross-linked by weak but abundant Zn(II)-carboxylate interactions, Nat. Commun. 9 (1) (2018) 2725.
[19] S. Burattini, B.W. Greenland, D.H. Merino, W. Weng, J. Seppala, H.M. Colquhoun, W. Hayes, M.E. Mackay, I.W. Hamley, S.J. Rowan, A healable supramolecular polymer Blend based on Aromatic π−π Stacking and hydrogen-bonding interactions, J. Am. Chem. Soc. 132 (34) (2010) 12051–12058.
[20] M. Capelot, D. Montarnal, F. Tournilhac, L. Leibler, Metal-catalyzed Transesterification for healing and assembling of Thermosets, J. Am. Chem. Soc. 134 (18) (2012) 7664–7667.
[21] J.P. Brutman, P.A. Delgado, M.A. Hillmyer, Polylactide Vitrimers, ACS Macro Lett. 3 (7) (2014) 607–610.

[22] Z.Q. Lei, H.P. Xiang, Y.J. Yuan, M.Z. Rong, M.Q. Zhang, Room-temperature self-healable and Remoldable cross-linked polymer based on the dynamic exchange of disulfide bonds, Chem. Mater. 26 (6) (2014) 2038–2046.
[23] S.M. Kim, H. Jeon, S.H. Shin, S.A. Park, J. Jegal, S.Y. Hwang, D.X. Oh, J. Park, Superior toughness and fast self-healing at room temperature engineered by transparent elastomers, Adv. Mater. 30 (1) (2017) 1705145.
[24] W.-X. Liu, C. Zhang, H. Zhang, N. Zhao, Z.-X. Yu, J. Xu, Oxime-Based and Catalyst-free dynamic covalent polyurethanes, J. Am. Chem. Soc. 139 (25) (2017) 8678–8684.
[25] D. Fu, W. Pu, Z. Wang, X. Lu, S. Sun, C. Yu, H. Xia, A facile dynamic crosslinked healable poly(oxime-urethane) elastomer with high elastic recovery and recyclability, J. Mater. Chem. A 6 (37) (2018) 18154–18164.
[26] Y. Cao, T.G. Morrissey, E. Acome, S.I. Allec, B.M. Wong, C. Keplinger, C. Wang, A transparent, self-healing, highly stretchable ionic conductor, Adv. Mater. 29 (10) (2017) 1605099.
[27] J. Xu, X. Zhu, J. Zhao, G. Ling, P. Zhang, Biomedical applications of supramolecular hydrogels with enhanced mechanical properties, Adv. Colloid Interface Sci. (2023) 321103000.
[28] L. Qiao, Y. Liang, J. Chen, Y. Huang, S.A. Alsareii, A.M. Alamri, F.A. Harraz, B. Guo, Antibacterial conductive self-healing hydrogel wound dressing with dual dynamic bonds promotes infected wound healing, Bioact. Mater. (2023) 30129–30141.
[29] S. Kalepu, V. Nekkanti, Insoluble drug delivery strategies: review of recent advances and business prospects, Acta Pharm. Sin. B 5 (5) (2015) 442–453.
[30] H. Guo, Y. Han, W. Zhao, J. Yang, L. Zhang, Universally autonomous self-healing elastomer with high stretchability, Nat. Commun. 11 (1) (2020) 2037.
[31] J. Kang, J.B.H. Tok, Z. Bao, Self-healing soft electronics, Nature Electronics 2 (4) (2019) 144–150.
[32] Y. Tu, N. Chen, C. Li, H. Liu, R. Zhu, S. Chen, Q. Xiao, J. Liu, S. Ramakrishna, L. He, Advances in injectable self-healing biomedical hydrogels, Acta Biomater. (2019) 901–920.
[33] M. Khatib, O. Zohar, H. Haick, Self-healing soft Sensors: from material Design to Implementation, Adv. Mater. 33 (11) (2021) 2004190.
[34] A. Rauf, M. Imran, M.S. Butt, M. Nadeem, D.G. Peters, M.S. Mubarak, Resveratrol as an anti-cancer agent: a review, Crit. Rev. Food Sci. Nutr. 58 (9) (2018) 1428–1447.
[35] A.P. Singh, R. Singh, S.S. Verma, V. Rai, C.H. Kaschula, P. Maiti, S.C. Gupta, Health benefits of resveratrol: Evidence from clinical studies, Med. Res. Rev. 39 (5) (2019) 1851–1891.
[36] T. Meng, D. Xiao, A. Muhammed, J. Deng, L. Chen, J. He, Anti-inflammatory action and mechanisms of resveratrol, Molecules 26 (1) (2021) 229.
[37] A.-L. Pignet, M. Schellnegger, A. Hecker, M. Kohlhauser, P. Kotzbeck, L.-P. Kamolz, Resveratrol-induced signal Transduction in wound healing, Int. J. Mol. Sci. 22 (23) (2021) 12614.
[38] W. Zhu, Y. Dong, P. Xu, Q. Pan, K. Jia, P. Jin, M. Zhou, Y. Xu, R. Guo, B. Cheng, A composite hydrogel containing resveratrol-laden nanoparticles and platelet-derived extracellular vesicles promotes wound healing in diabetic mice, Acta Biomater. (2022) 154212–154230.
[39] Y. Zheng, W. Yuan, H. Liu, S. Huang, L. Bian, R. Guo, Injectable supramolecular gelatin hydrogel loading of resveratrol and histatin-1 for burn wound therapy, Biomater. Sci. 8 (17) (2020) 4810–4820.
[40] İ. Eroğlu, E.H. Gökçe, N. Tsapis, S.T. Tanrıverdi, G. Gökçe, E. Fattal, Ö. Özer, Evaluation of characteristics and in vitro antioxidant properties of RSV loaded hyaluronic acid–DPPC microparticles as a wound healing system, Colloids Surf. B Biointerfaces (2015) 12650–12657.
[41] G. Yang, Z. Zhang, K. Liu, X. Ji, P. Fatehi, J. Chen, A cellulose nanofibril-reinforced hydrogel with robust mechanical, self-healing, pH-responsive and antibacterial characteristics for wound dressing applications, J. Nanobiotechnol. 20 (1) (2022).
[42] S. Huang, D. Lei, Q. Yang, Y. Yang, C. Jiang, H. Shi, B. Qian, Q. Long, W. Chen, Y. Chen, L. Zhu, W. Yang, L. Wang, W. Hai, Q. Zhao, Z. You, Y. Xiaofeng, A perfusable multi-functional epicardial device improves cardiac function and tissue repair, Nat. Med. 27 (3) (2021) 480–490.
[43] S. Wang, B. Luo, B. Bai, Q. Wang, H. Chen, X. Tan, Z. Tang, S. Shen, H. Zhou, Z. You, G. Zhou, D. Lei, 3D Printed Chondrogenic Functionalized PGS Bioactive Scaffold for Cartilage regeneration, Adv. Healthcare Mater. 12 (27) (2023) 2301006.
[44] R. Yu, M. Li, Z. Li, G. Pan, Y. Liang, B. Guo, Supramolecular Thermo-Contracting adhesive hydrogel with self-Removability simultaneously enhancing Noninvasive wound closure and MRSA-infected wound healing, Adv. Healthcare Mater. 11 (13) (2022).
[45] D. Zhang, G. Cai, S. Mukherjee, Y. Sun, C. Wang, B. Mai, K. Liu, C. Yang, Y. Elastic Chen, Persistently Moisture-Retentive, and Wearable biomimetic film inspired by Fetal Scarless repair for promoting skin wound healing, ACS Appl. Mater. Interfaces 12 (5) (2020) 5542–5556.
[46] K. A, L. A, Mechanical Behaviour of skin: a review, J. Mater. Sci. Eng. 5 (4) (2016) 1000254.
[47] S. Chen, L. Sun, X. Zhou, Y. Guo, J. Song, S. Qian, Z. Liu, Q. Guan, Jeffries E. Meade, W. Liu, Y. Wang, C. He, Z. You, Mechanically and biologically skin-like elastomers for bio-integrated electronics, Nat. Commun. 11 (1) (2020) 1107.
[48] H. Wu, P. Yang, A. Li, X. Jin, Z. Zhang, H. Lv, Chlorella sp.-ameliorated undesirable microenvironment promotes diabetic wound healing, Acta Pharm. Sin. B 13 (1) (2023) 410–424.
[49] X. Huang, J. Sun, G. Chen, C. Niu, Y. Wang, C. Zhao, J. Sun, H. Huang, S. Huang, Y. Liang, Y. Shen, W. Cong, L. Jin, Z. Zhu, Resveratrol promotes diabetic wound healing via SIRT1-FOXO1-c-Myc Signaling Pathway-mediated angiogenesis, Front. Pharmacol. (2019) 1000421.
[50] Xia Li, Daiber Hasselwander, Resveratrol and vascular function, Int. J. Mol. Sci. 20 (9) (2019) 2155.
[51] C.-C. Zhao, L. Zhu, Z. Wu, R. Yang, N. Xu, L. Liang, Resveratrol-loaded peptide-hydrogels inhibit scar formation in wound healing through suppressing inflammation, Regenerative Biomaterials 1 (2019) 99–107.
[52] E. Gokce, Dellera Korkmaz, Bonferoni Sandri, O. Ozer, Resveratrol-loaded solid lipid nanoparticles versus nanostructured lipid carriers: evaluation of antioxidant potential for dermal applications, Int. J. Nanomed. (2012) 71841–71850.
[53] X. Zhao, Y. Liang, Y. Huang, J. He, Y. Han, B. Guo, Physical Double-network hydrogel adhesives with rapid Shape Adaptability, fast self-healing, antioxidant and NIR/pH Stimulus-Responsiveness for Multidrug-resistant Bacterial Infection and removable wound dressing, Adv. Funct. Mater. 30 (17) (2020) 1910748.